Image Properties Prediction in Nonlinear Model-based Reconstruction using a Perceptron Network

Wenying Wang, J. Webster Stayman, and Grace J. Gang

Department of Biomedical Engineering, Johns Hopkins University, Baltimore, MD, 21205

Abstract Nonlinear reconstruction algorithms have demonstrated superior resolution to noise tradeoffs compared to traditional linear reconstruction methods. However, their nonlinear, shift variant, and data-dependent nature complicates performance analysis. Furthermore, there usually lacks a predictive framework for image properties that allows efficient control and optimization of imaging performance. In this work, we quantify the system response of general nonlinear reconstructions using a quantitative perturbation response metric and develop a data-driven approach for prospective prediction of such properties as a function of varying perturbations (size, shape, contrast, and contrast profile), patient anatomy, and algorithmic parameter. The feasibility of prediction framework is demonstrated for a penalized-likelihood reconstruction algorithm with a Huber penalty (PLH). We incorporated a compact representation of the imaging system and the perturbation as the input to the network and used a three-layer perceptron network for image property prediction. The predicted perturbation response shows good agreement with those obtained from empirical measurements. The prediction accuracy is generalizable to all perturbations, anatomical locations, and regularization parameters investigated. Results in this work suggest that the data-driven method and training strategies developed herein is a promising approach for prospective image property prediction and control in nonlinear reconstruction algorithms.

1 Introduction

The recent proliferation of nonlinear reconstruction algorithms have presented tremendous opportunities for image quality improvement and dose reduction. However, despite promising results in the research setting, clinical translation of these algorithms have met a number of challenges. Due to their nonlinear, shift-variant, and data-dependent nature, traditional image quality assessment metrics rooted in linear system analysis (e.g., impulse response, noise power spectrum) may no longer apply. For example, the appearance of a lesion of interest in an MBIR reconstructed image can be highly dependent on its location in the anatomy. Lesions of different contrast may also result in different edge profiles [1]. Furthermore, the performance of nonlinear algorithms often rely on careful tuning of algorithmic parameters (e.g., regularization strength). The relationship between these parameters and image properties, however, is often opaque. As a result, image properties are often analyzed in a *retrospective* fashion via empirical measurements. Optimization of nonlinear algorithms therefore frequently relies on exhaustive evaluations overs the parameters of interest, which is time consuming due to the large number of dependencies mentioned previously.

In previous work [2, 3], we proposed a novel image quality analysis framework capable of *prospective* predictions of image properties in general nonlinear reconstruction algorithms. Leveraging the universal approximation theorem, we trained an artificial neural networks model to map the nonlinear transfer functions of an example model-based reconstruction algorithm. In this work, we present further development of the framework focusing on efficient training strategies that allows the predictive capability of the model to be generalized to arbitrary stimuli, anatomy, and imaging conditions.

2 Materials and Methods

2.1 Generalized system response

In linear shift-invariant imaging systems, the system response can simply be characterized by the impulse response function which is dependent on the system parameters, $\mathbf{S}$. For general nonlinear algorithms, the system response carries additional dependencies on the measurement data, y, and the stimulus/perturbation, μ_s. Following Ahn and Leahy[4], we define the generalized system response of a reconstruction algorithm, $\mathscr{H}(\mu_s;\mu,\mathbf{S})$, as the difference between the mean reconstructions ($\hat{\mu}$) with and without the perturbation:

$$\mathscr{H}(\mu_s;\mu) = \overline{\hat{\mu}(y(\mu+\mu_s;\mathbf{S}))} - \overline{\hat{\mu}(y(\mu;\mathbf{S}))}. \tag{1}$$

The generalized system response extends the characterization of the dependencies on the background anatomy μ and the stimuli μ_s introduced in nonlinear algorithms in addition to the dependencies on imaging system characterizations and reconstruction approach including regularization designs demonstrated in locally linearizable algorithms.

2.2 Penalized-likelihood reconstruction with a Huber penalty

In this work, we demonstrate methods for developing the predictive analysis framework on an example MBIR algorithm based on a penalized-likelihood objective with a Huber penalty. The objective function is given by:

$$\Phi(\mu,y) = L(\mu;y) - R(\mu,\beta,\delta) \tag{2}$$

where $L(\mu;y)$ is the log-likelihood term that presumes the measurements follow an independent Poisson distribution, and $R(\mu,\beta,\delta)$ is the Huber penalty active in the 4-nearest neighborhood:

$$R(\mu,\beta,\delta) = \beta \sum_j \sum_{k\in\mathscr{N}_j} \phi_H(\mu_j-\mu_k;\delta) \tag{3}$$

$$\phi_H(x;\delta) = \begin{cases} \frac{x^2}{2\delta}, & |x|\le\delta \\ |x|-\frac{\delta}{2}, & |x|>\delta \end{cases} \tag{4}$$

The term contains two regularization parameters, where β controls the overall regularization strength and δ controls the threshold in voxel differences where the potential function transitions from quadratic to linear. The interaction between β and δ results in a complex tradeoff between overall smoothness and edge preservation. Examples of such dependencies

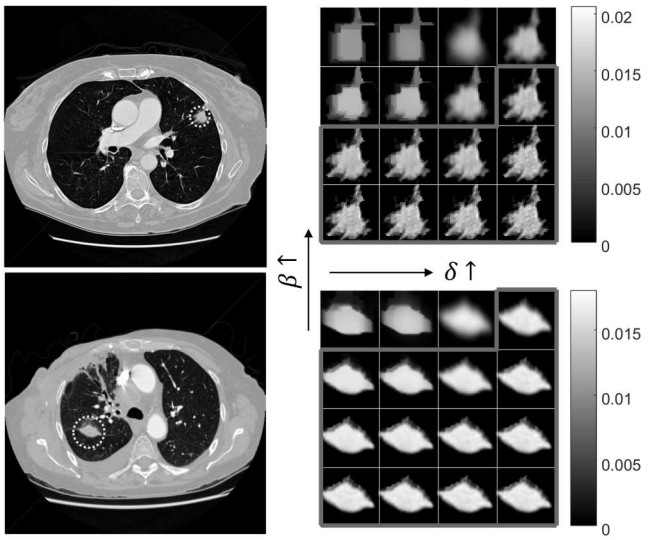

Figure 1: Generalized system response of two lung nodules with different regularization values. The green line circumscribes the "good" perturbation responses. (Unit: mm^{-1})

are illustrated in Figure 1 with two lung nodules in the Lung Image Database Consortium (LIDC) [5]. Each subplot on the right shows the generalized system response (Eq.1) corresponding to PLH reconstructions at different combinations of β and δ. From visual inspection, the perturbation response can be distorted with poor regularization parameters combinations. Moreover, because the system is nonlinear, a set of regularization parameters that can achieve good response with one perturbation may not work for other perturbations. The spiculated lung nodule (top) shows less tolerance of high regularization strength compared to the smooth lung nodule (bottom). As a quantitative measure of how faithfully nodules are represented in the reconstructions, we circumscribed the region of "good" (β, δ) where the perturbation response has less than 30% relative root mean square error (rRMSE) compared to the ground truth (rRMSE is defined as the normalized RMSE over the root mean square of the ground truth). While the regions in Fig.1 were identified through empirical measurements, the following sections aim to establish a model to predict perturbation responses without the need for reconstructions.

2.3 Prediction Framework Implementation

The prediction framework leverages the universal approximation theorem which states that a fully-connected neural network with a single hidden layer that is of arbitrary number of nodes or an arbitrarily deep fully-connected network with a finite number of nodes in each hidden layer can approximate any well-behaved continuous function $f : \mathbb{R}^d \rightarrow \mathbb{R}^D$ with a arbitrarily small residual distance.[6, 7] In this section, we discuss the efficient information for perturbation response prediction, space sampling strategy, and prediction neural network architecture setup.

2.3.1 Efficient information for prediction

We leveraged prior knowledge of the image properties of PLH to devise efficient network inputs. Ahn and Leahy [4] derived an explicit closed-form expression of the perturbation response in locally linearizable algorithms:

$$\mathscr{H}(\mu_s) = [\mathbf{A}^T\mathbf{W}\mathbf{A} + \mathbf{R}]^{-1}\mathbf{A}^T\mathbf{W}\mathbf{A}\mu_s \tag{5}$$

where $\mathbf{W}$ is the covariance matrix of the measurements and $\mathbf{R}$ denotes the Hessian of the regularizer. For Huber penalty, the Hessian term is image dependent and therefore difficult to evaluate. However, the Fisher information term $\mathbf{A}^T\mathbf{W}\mathbf{A}\mu_s$ efficiently characterizes the dependencies on system geometry (through $\mathbf{A}$), data statistics (through $\mathbf{W}$), and perturbation (through μ_s). Therefore, as a compact representation of the imaging system, the anatomical background, and the perturbation, the Fischer information term $\mathbf{A}^T\mathbf{W}\mathbf{A}\mu_s$ along with the regularization parameters are used as inputs to the network to provide sufficient information to determine the generalized system response of the PLH. This expression also informs the range of training data required to achieve generalizable predictive capability.

2.3.2 Parameter space sampling in training data

In a data-driven method, the range of training data is directly related to network performance. In this work, we seek to build a predictive model for the generalized system response as a function of (A) perturbation, (B) background anatomy and locations, and (C) regularization. We propose the following sampling strategies for each parameter in the context of lung imaging:

(A) Sampling the perturbation (μ_s): The perturbations, or lung lesions, have large variabilities in terms of their size, contrast, shape, and contrast profiles. To efficiently sample the perturbations, we adopted a parametric model for realistic lesion simulation developed by Solomon and Samei [8]:

$$c(\theta, r) = C(1 - (r/R_\theta)^2)^n \tag{6}$$

where C is the peak contrast value, n describes the steepness of the profile, and R_θ is the distance from the center to the edge along the radial direction θ. This type of model allows us to systematically represent perturbations by sampling combinations of (C, n, R_θ). We sampled scalars C and n with the range described in [8]. For the vector R_θ, we sampled R_θ along 8 radial directions according to a normal distribution of mean $\bar{R}$ and variance σ_R), and used interpolation to achieve smoothly varying R_θ for arbitrary θ.

(B) Sampling the anatomy and locations (W): We used the XCAT chest digital phantom [9] as the background anatomy in the simulation study and manually selected locations to insert lesions. These locations represent various profiles of statistical weights $\mathbf{W}$ pertaining to lung imaging.

(C) Sampling the regularization (β,δ): We sampled the different combinations of regularization parameters (β, δ) using a 2D sweep. The range of the regularization parameters are selected to sufficiently include a variety of reconstruction outcomes illustrated in Fig.1.

2.3.3 Efficient network architecture

With the efficient input proposed in Sec. 2.3.1, we seek to approximate the following function with a neural network:

$$\mathscr{H}(\mu_s, \mu) = f(\mathrm{ROI}[\mathbf{A}^T\mathbf{W}\mathbf{A}\mu_s], \beta, \delta). \tag{7}$$

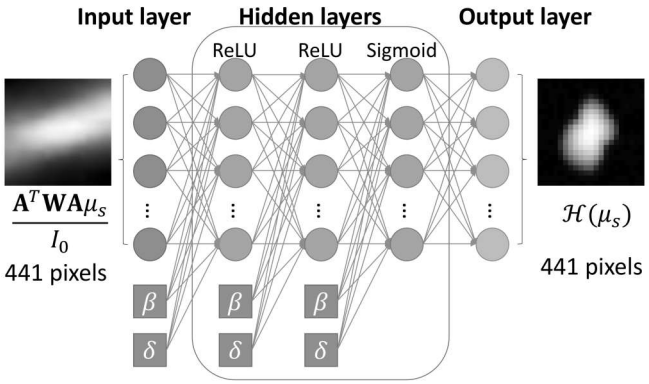

Figure 2: Structure of the multi-layer perceptron neural network.

Dataset	C (HU)	n	$\bar{R}$(mm)	$\sigma_R/\bar{R}$
Training	600:200:1400	0.5,0.75,1.0	3,4,5,6	0.2,0.5
Testing	700,1100	0.6,0.9	3.5,4.5,5.5	0.35

Dataset	$\log(\beta)$	$\log(\delta)$
Training	2.0:0.8:6.0	2.4:0.8:5.6
Testing	-5.0:0.8:-1.0	-4.6:0.8:-1.4

Table 1: Lesion synthesis and regularization parameters in data generation.

According to the universal approximation theorem, a perceptron network with a single hidden layer can approximate arbitrary functions give enough nodes in the hidden layer. When using more hidden layers, each layer requires a smaller number of nodes. Through empirical experimentation, we adopt a perceptron network that has three hidden layers as shown in Figure 2. The input stacks the Fisher information term the regularization parameters. The corresponding output is the measured system response as the difference between PLH reconstructions with the perturbation and without the perturbation. Furthermore, for this investigation, we assumed a well-sampled imaging geometry where the perturbation response is contained in a local region. This assumption allows us to truncate $\mathbf{A}^T\mathbf{W}\mathbf{A}\mu_s$ and μ_s to reduce the dimensionality of the network. All Fisher information term ($\mathbf{A}^T\mathbf{W}\mathbf{A}\mu_s$) and outputs ($\mathscr{H}(\mu_s,\mu)$) of the network is contained with in a 21x21 grid. Each hidden layer has 441 nodes that is of the same size as the output layer. To feed the regularization parameters to the network, we concatenate (β,δ) to the first two hidden layer. All nodes are fully connected. The first two layer is activated with a rectified linear unit (ReLU), and the last layer with a sigmoid function.

2.4 Experiment setup

Following the sampling strategies proposed in Sec. 2.3.2, we generated training and testing datasets according to the various dependent parameters. The lung nodule parameters and (β,δ) are shown in Table 1. With each set of parameters, we generated 50 nodules for training and 10 nodules for testing, resulting in 6000 nodules in the training dataset and 120 nodules in testing dataset. Figure 3 illustrates example nodules corresponding to nodule parameters in both training and testing. The simulated lung lesions are inserted in 19 locations on a 2D slice in the chest phantom as shown in Fig.4. For initial investigation, we performed training and testing on the same anatomical background. Generalizing the prediction framework to varying anatomical background is the subject of ongoing work.

The perceptron neural network was trained by minimizing the mean square error between the predicted perturbation responses and the measurements using the ADAM optimizer. Prediction feasibility was validated through qualitative comparison and quantitative evaluation using structural similarity index measure (SSIM). We raised one example application of the proposed prediction framework in efficient prospective regularization selection, where the boundaries of proper regularizations that can produce "good response" with small rRMSE (akin to Fig. 1) were determined using measured response through a retrospective exhaustive parameters sweep or prospective evaluation using the prediction model. The comparison between the measured and predicted boundaries demonstrated the efficacy of prospective approach.

3 Results

Prediction accuracy of the proposed framework was validated through comparisons between predicted and measured perturbation responses. Pairs of measurement and prediction are shown in Figure 5 with varying regularization parameters (β, δ), perturbations, and locations, respectively. The predictions show good agreement with the measurements and are capable of characterizing all dependencies investigated. The agreement between prediction and measurement is further quantified in terms of the SSIM metric. The mean SSIM among all testing cases is 0.9991. Over 99% of the predictions achieves 0.995 of SSIM when compared to the measured ground truth.

An example application of the proposed predictor is demonstrated in efficient selection of "good" regions of regularization parameters, i.e., a quantitative alternative to Fig.1 without the need for additional reconstructions. Figure 6 shows two maps of rRMSE with varying regularization combinations. The ground truth plot (top left) were computed from measured perturbation response through an exhaustive sweep. The bottom left plot shows the predicted rRMSE map computed with finer sampling of regularization parameters. The green lines circumscribed the "good response" areas where the rRMSE is smaller than 30%. The plots on the right show two examples of perturbation responses from the "good response" region circumscribed in green and the "bad response" region circumscribed in red. We notice that despite the predicted rRMSE values deviate from the measured values in the highly-regularized region, the predicted "good response" region shows great agreement with the outcome of retrospective evaluation, demonstrating the capability of using this predictor for regularization parameters selection.

4 Discussion and Conclusion

In this work, we propose a prediction framework that quantifies the perturbation response of a nonlinear reconstruction algorithm, where a multi-layer perceptron network is used to approximate the perturbation response in a data-driven

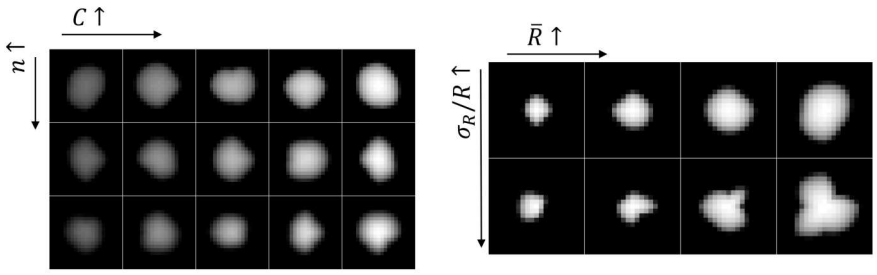

Figure 3: Examples of synthesized lung nodules for training.

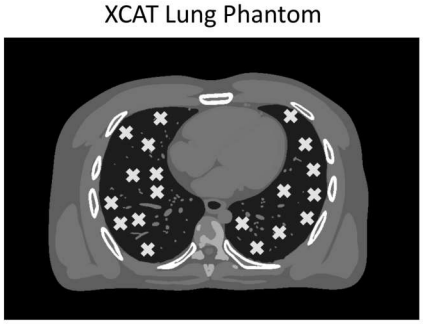

Figure 4: XCAT simulated anatomical background. The yellow crosses indicate the locations to insert perturbations.

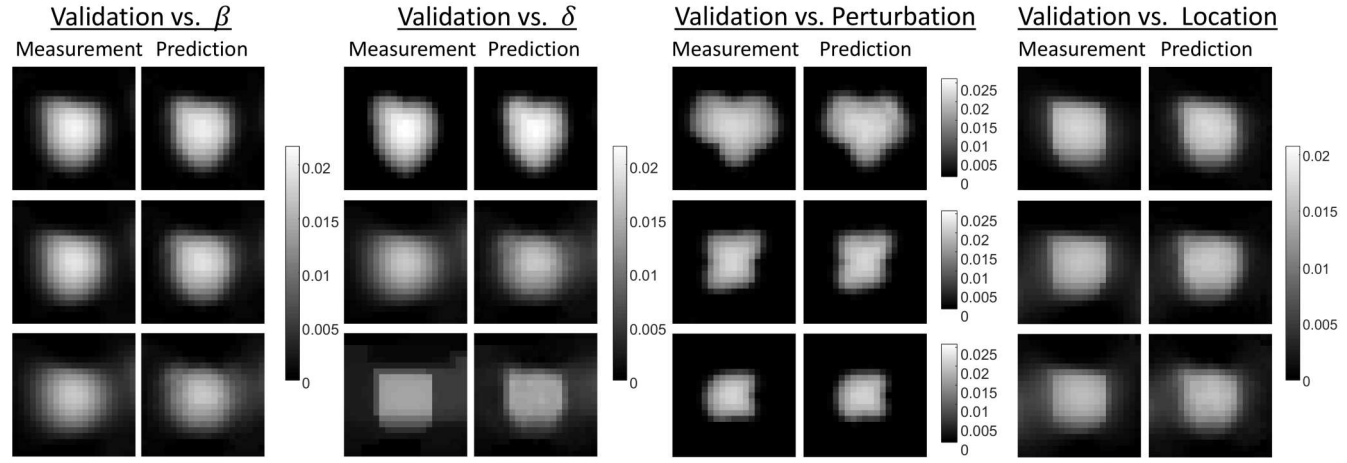

Figure 5: Comparisons between measurements and predictions with varying regularizations, perturbations, and locations. Unit: mm^{-1}.

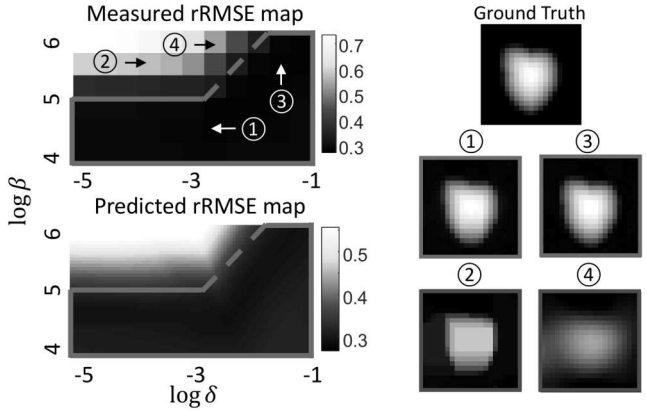

Figure 6: Measured and predicted rRMSE map with varying β and δ. The regularization parameter combinations are circumscribed with green lines. Examples of perturbation responses are shown on the right.

fashion. We establish a sampling strategy to guarantee good characterization of the perturbation dependencies on regularization parameters, perturbation features, and locations. We demonstrate the feasibility of the prediction framework in simulation study, and show the potential application of the tool towards regularization tuning for reliable system response. Ongoing work includes incorporating variability in background anatomy and refine the perturbation model to achieve good agreement for more realistic perturbations in clinical dataset.

Acknowledgement

This work is supported, in part, by NIH grants R01CA249538 and R01EB027127.

References

[1] Richard, S *et al.*, *Medical physics*, vol. 39, no. 7, pp. 4115–22, 2012.

[2] Gang, G. J *et al.*, in *Medical Imaging 2019: Physics of Medical Imaging*, Bosmans, H *et al.*, Eds., no. March. SPIE, mar 2019, p. 20.

[3] Wang, W *et al.*, in *6th International Conference on Image Formation in X-Ray Computed Tomography*, 2020, pp. 1–4.

[4] Ahn, S and Leahy, R. M, *IEEE Transactions on Medical Imaging*, vol. 27, no. 3, pp. 413–424, 2008.

[5] Hancock, M. C and Magnan, J. F, *Journal of Medical Imaging*, vol. 3, no. 4, p. 044504, 2016.

[6] Cybenko, G, *Mathematics of Control, Signals, and Systems*, vol. 2, no. 4, pp. 303–314, dec 1989.

[7] Lu, Z *et al.*, in *Advances in Neural Information Processing Systems*, Guyon, I *et al.*, Eds., vol. 30. Curran Associates, Inc., 2017, pp. 6231–6239.

[8] Solomon, J and Samei, E, *Physics in Medicine and Biology*, vol. 59, no. 21, pp. 6637–6657, 2014.

[9] Segars, W. P *et al.*, *Medical Physics*, vol. 37, no. 9, pp. 4902–4915, 2010.